Large Amplitude Gravity Waves above Southern Andes, Drake Passage and Antarctic Peninsula

A. de la Torre[1], P. Alexander[2], R. Hierro[1], P. Llamedo[1], A. Rolla[1], T. Schmidt[3] and J. Wickert[3]

[1] A. de la Torre, R. Hierro, P. Llamedo, A. Rolla, Facultad de Ingeniería, Universidad Austral, Avda. Garay 125, 5to Piso, C1063ABB Buenos Aires, Argentina (Adelatorre@austral.edu.ar, Rhierro@austral.edu.ar, Pllamedo@austral.edu.ar, Arolla@austral.edu.ar)

[2] P. Alexander, Departamento de Física, Facultad de Ciencias Exactas y Naturales, Universidad de Buenos Aires, Ciudad Universitaria, 1428 Buenos Aires, Argentina (peter@df.uba.ar)

[3] T. Schmidt and J. Wickert, Helmholtz Centre Potsdam, GFZ German Research Centre for Geosciences, Telegrafenberg A17, Potsdam, D-14473, Germany (tschmidt@gfz-potsdam.de)(wickert@gfz-potsdam.de).

Abstract.

Previously to a research program to be accomplished during winter 2013 along Southern Andes Range and its prolongation in the Antarctic Peninsula (Southern Andes - ANtarctic GRavity wave InitiAtive (SAANGRIA)), large amplitude mountain and shear gravity waves observed with Weather Research and Forecasting (WRF) mesoscale model simulations during winter 2009 are analyzed. The simulations are forced with Era-Interim data. The approach selected for the regional downscaling is consecutive integrations with weekly reinitialization with 24 hours of spin-up and the outputs during this period are excluded from the analysis. From June 1 to August 31, 5 cases study were selected on the basis of their outstanding characteristics and large wave amplitudes. The complete period analyzed suggests that the 5 racetracks proposed for the SAANGRIA experiment are representative of the typical mountain wave morphology in the region. In general, one or two prevailing modes of oscillation are identified after applying continuous wavelet transforms at constant latitudes and pressure levels. In all cases, the prevailing modes are characterized by horizontal and vertical wavelengths around or shorter than 100 km and longer than 8 km respectively. Regional and synoptic conditions for each case are described. The zonal and meridional components of the vertical flux of horizontal momentum is calculated for one of the cases, considering a broad wave spectrum and in particular the prevailing wave. A large relative contribution to this flux due to short horizontal wavelengths of the spectrum is observed in comparison with the momentum

only transported by the prevailing mode, in agreement with theoretical results.

1. Introduction

Internal gravity waves (GWs) play a very important role in many dynamical and plasma processes extending from Earth's surface upward into the thermosphere and ionosphere. They are major contributors to the atmospheric structure and produce effects that impact the atmosphere at essentially all altitudes and all spatial and temporal scales. Main GW sources are found in the troposphere and lower stratosphere [*e.g. Fritts and Alexander*, 2003]. GWs drag in general circulation models has been usually treated with parameterizations. These models, due to their spatial and temporal resolutions, cannot explicitly resolve subgrid GWs phenomenons like GWs drag. A primary limitation of the development and validation of these representations has been the lack of observational constraints on waves. Moreover, it is very difficult to obtain a complete view of three-dimensional time-varying atmospheric processes with a single instrument or technique [*Wu et al*, 2006]. Radiosonde, lidar, radar, and rocket measurements generally provide local observations of GWs, whereas measurements on board satellites can yield global coverage. Nevertheless, our understanding of GW dynamics and their effects still remains seriously deficient in important areas.

In particular, GWs generated by flow over mountains have strong impacts on mesoscale circulation, precipitation and turbulence occurrence and intensity. Large terrain features such as mountain ranges create mountain waves (MW) that transport energy and mean-flow horizontal momentum away from the lower atmosphere towards the middle and upper atmosphere, where they are deposited. It is now recognized that this deposition of energy and momentum is an essential component of the global circulation. Short and mesoscale

GWs contribute largely to the momentum balance of the stratosphere [*e.g.* *Fritts and Alexander*, 2003].

Horizontal momentum is transported by MWs from the region of wave dissipation to the surface, where a net pressure force is exerted by Newton's third law on the topography. A decelerative force is exerted on the large scale atmospheric circulation in those regions where the wave undergoes dissipation. The basic structure of a MW is determined by the size and shape of the mountains, by the vertical profiles and lapse rates of temperature (T), wind speed and moisture in the impinging flow [*e.g.* *Gill*, 1982]. Non linear effects do exert a significant influence on the wave amplitude and are essential to the dynamics of MW dissipation in regions of wave breaking by overturning. As it is known, the largest momentum fluxes ($\boldsymbol{M}$) are carried by those waves with short horizontal (λ_x) and long vertical wavelengths (λ_z) [*e.g.* *Preusse et al*, 2008]. The effects of this deposition of momentum (sometimes called drag or stress) on the atmosphere are profound and important on all scales of flow. For example, the quasibiennial and semiannual oscillations in equatorial zonal winds are at least partially driven by the convergence of $\boldsymbol{M}$ carried by GWs [*e.g.* *Ern et al*, 2004, and references therein]. An early direct observation of $\boldsymbol{M}$ (in the mesosphere) by GWs was made by *Vincent and Reid* [1983] using a split beam technique with an HF radar.

We now know that the region close to Southern Andes, Drake Passage and Antarctic Peninsula during winter is one of the most energetic region on Earth for the deep vertical propagation of GWs. It exhibits among the largest, if not the largest, mesoscale (10 to 1000 km) variability at altitudes from 20 to 60 km of any region on Earth [*e.g.* *Plougonven et al.*, 2008; *Shutts and Vosper*, 2011]. In situ measurements with 24 superpressure balloons released from McMurdo (Antarctica) during spring 2005 allowed to measure the absolute momentum flux ($|\boldsymbol{M}|$) distribution at floatation levels [*Vincent et al*, 2007; *Hertzog et al*, 2008]). The longest Vorcore flight lasted 109 days and the mean flight duration during the campaign was about 59 days. At constant pressure levels, the overall campaign averaged $|\boldsymbol{M}|$ was 2.5 mPa, whereas above the Antartic peninsula in a 10 deg latitude per 5 deg longitude region reached 28 mPa. The zonal component of $\boldsymbol{M}$ was observed negative almost everywhere, which indicates that the vast majority of GW were propagating against the mean eastward flow characteristic of the wintertime stratosphere. The largest westward values were found above or in the lee of major orography. In general, the fluxes were detected to be largely westward, but significant localized meridional values also occurred over the topography.

Remote sensing measurements from limb scanning satellite data allowed to derive T vertical profiles. These provide a low level limit to $|\boldsymbol{M}|$, under specific theoretical constraints [*see e.g. Ern et al, 2004*]. A critical point here consists in the accurate determination of the horizontal component of the wavenumber vector associated to the prevailing GW mode that effectively contributes to $|\boldsymbol{M}|$. From Cryogenic Infrared Spectrometers and Telescopes for the Atmosphere (CRISTA) data during August 1997 and at 25 km height, $|\boldsymbol{M}|$ values between 2.5 and 25 mPa were found. More recently, from High Resolution Dynamics Limb Sounder (HIRDLS) data, *Alexander et al* [2008] obtained global estimates of $\boldsymbol{M}$, averaged between 20 and 30 km height for the single day 16 May 2006, reporting values between 2.5 and 5 mPa in the southern tip of the Andes Range. T soundings from the Constellation Observing System for Meteorology, Ionosphere, and Climate and Challenging Minisatellite Payload GPS RO missions (COSMIC and CHAMP) were used to derive

$|\boldsymbol{M}|$ in the altitude range of 17.5 and 22.5 km during December 2006 to February 2007 [*Wang and Alexander*, 2010]. Similar values to those reported in previous studies in the region considered by *Ern et al* [2004] and *Alexander et al* [2008], averaged in the altitude range of 17.5 and 22.5 km during December 2006 to February 2007 were obtained. From nadir scanning satellite T data with the Atmospheric Infrared Sounder (AIRS), an event of 140 mPa at 40 km height with $\lambda_h = 300$ km and $\lambda_z = 20$ km was detected [*Alexander and Teitelbaum*, 2007]. With this same instrument, events over S. Georgia were described in *Alexander et al* [2009], including a range of λ_h between 50 and 400 km and averaged over a 2.5 deg latitude per 2.5 deg longitude area. $|\boldsymbol{M}|$ ranging between 60 and 200 mPa were reported, with local values greater than 1000 mPa.

A research program combining new measurements spanning altitudes from Earth's surface to the mesopause, with mesoscale models able to describe GW dynamics and effects from turbulence to planetary scales, has been proposed [*Smith et al*, 2008]. The Southern Andes ANtarctic GRavity wave InitiAtive (SAANGRIA) project, includes a field measurement campaign planned from June to September 2013 to study the dynamics of GW in the Southern Andes-Antarctic Peninsula region, from the surface of the earth to the mesosphere and lower thermosphere (MLT). The project is proposed to occur during winter, in coincidence with the maximum in GW activity and its apparent influence in the stratosphere, mesosphere and lower thermosphere. Main objectives of this project are:

- detailed measurements and modelling of GW dynamics, including their sources, propagation, instabilities and effects, from the troposphere to the MLT, in the GW "natural laboratory" region spanning the southern Andes, Drake Passage and Antarctic Peninsula;

- analysis of GW variations with altitude, including filtering and interactions throughout the stratosphere largely above the major sources and the implications for vortex-edge drag and polar stratospheric clouds occurrence and ozone depletion over the Antarctic Peninsula, both of first-order relevance to climate models;

- propagation, filtering, and nonlinear interaction studies addressing GW (and MW) penetration into the MLT, where filtering by tidal and planetary wave motions, interactions and instabilities and mean flow and large-scale forcing play major roles in the circulation, structure and variability; and

- fundamental predictability studies of MWs and GWs and their secondary effects, which will guide improvements in GW prediction and parameterizations in applications for numerical weather prediction, climate, and general circulation modelling communities.

In section 2 we describe the numerical simulations and their validation with experimental radio occultation T profiles; in section 3 the wave analysis performed is described for each of the 5 cases considered; in section 4, a detailed calculation of $\boldsymbol{M}$ for one (for brevity) of the selected cases is presented, and in section 5 some conclusions are outlined.

2. Numerical Simulations

In five representative examples during winter 2009, we describe simulations using the Weather Research and Forecasting (WRF 3.0) regional model [*Skamarock et al*, 2008]. The regional circulation and the vertical (w), zonal (u) and meridional (v) velocity and T fields before and during the development of these events, were determined. The simulations are forced with ERA-Interim data to construct initial and boundary conditions. The approach selected for the regional downscaling is consecutive integrations with weekly reinitialization with 24 hours of spin-up and the outputs during this period are excluded from the analysis. Each reinitialization runs for 8 days whose total integration tiem spans the integration periods selected [*von Storch et al*, 2000]. They are carried out in three different regions of interest (Figure 1) with 50 vertical levels (from 1000 to 50 hPa every 50 hPa, from 50 to 10 hPa each 10 hPa and from 10 to 1 hPa every 1 hPa), 2.75 km meridional resolution and a zonal resolution ranging from 2 km (at 47S) to 1.3 km (at 72S). Synoptic conditions are obtained from global ERAInterim data fields. The dates selected from June, July and August 2009 correspond below to cases 1 to 5 (07/16, 06/25, 06/21, 07/28 and 07/19, respectively). Each date was selected by its outstanding wave amplitude. In particular we describe the structure observed as a function of height along the 5 constant latitude proposed aircraft racetracks during the SAANGRIA experiment. These racetracks, chosen above the mountain tops and the Drake Passage, roughly correspond to latitudes 49, 54, 59, 65 and 71S, (cases 1 to 5 respectively).

To validate the simulations, available T GPS-COSMIC (Global Positioning System-Constellation Observing System for Meteorology, Ionosphere and Climate) radio occultation (RO) profiles are used for the 5 cases considered (Figure 2). The individual data belonging to each RO profile generate a so-called line of tangent points (LTP) (solid lines). The upper limit and ground level corresponding to each LTP are horizontally separated up to 100 km. This may result in an atmospheric sounded region quite different from the vertical direction. In Figure 2, dashed lines represent the WRF T simulation, interpolated along the corresponding LTPs. In the 5 cases, 50 pairs of points are considered and the calculated linear correlation coefficient is always greater than 0.99. The probability that these high correlation coefficients is a by-product of chance (Hypothesis Test performed) is lower than 0.0001.

3. Wave analysis

The 3-D nature of GW signatures allows the wave analysis along vertical, horizontal or even slanted directions. In our case, due to the characteristics of the region under study, with expected dominant high and moderate intrinsic frequency modes, we analyze the zonal variability at fixed latitudes and standard tropospheric and stratospheric pressure levels. The horizontal resolution available at each domain is sufficient for typical λ_x longer than 30-40 km, according to previous analyses in the region [*e.g. de la Torre et al*, 2006]. To isolate dominant spectral components, a Morlet continuous wavelet transform (CWT) is applied to $w(x)$. A basic capability of a CWT analysis is the localization of main modes of oscillation in restricted intervals of the data series. These are expected to take place near the mountainous regions in cases 1, 2, 4 and 5. λ_x for each dominant mode is expected to be mostly preserved throughout the troposphere. Due to refraction effects, this is not the case for λ_z, in the numerical simulations ground referred inertial frame.

w constitutes an appropriate dynamical variable to evidence the presence of MWs (e.g. Smith, 1979; Shutts et al, 1988). To apply the CWT analysis, we first consider horizontal zonal profiles at standard pressure levels in domains 1, 2 and 3 respectively, regularly spaced -zonal profiles (ZP)-. A nonrecursive high-pass filter with a Kaiser window (e.g., Hamming, 1998) and a cutoff at 360 km is applied to each ZP^w to remove the background. Subtracting filtered from not filtered ZP, we obtain $\mathrm{ZP}^{<360}$, or simply, $w_{<360}$. The filter is applied again with cutoff at 8 km and aliasing effects are eliminated, thus obtaining each band-passed w_{bp} between 8 and 360 km.

3.1. Case 1 (49S)

The event (Figure 3a) is characterized by a low pressure system crossing the Drake Passage at 06Z while at this time in the upper troposphere a long wave trough is located over Pacific Ocean, yielding a NW-SE circulation over Patagonia and most of Drake (Figure 3b). It is possible to see that both the pressure system and the upper level trough are not in phase taking place a west tilting with height. However, over Patagonia, the low level flow as well as the upper level flow present a NW-SE circulation because of the position of the NE region of the cyclone in the former and the long wave trough in the latter. As a result, the component of rotation in wind shear seems not to be important, keeping the same wind direction from low to upper level in the troposphere (Figures 3c-d). A propagating large amplitude and stationary structure forced by the mountains up to the stratosphere, persistent during at least 12 hours is observed (Figure 4a-b). A predominant λ_x around 100 km (CWT at 600 hPa) and long λ_z (near to 10 km) is clear (Figure 4c). A closer insight shows the variation in CWT for seven arbitrary consecutive directions (Figure 4d), starting from the zonal direction and the intersection between ZP with the maximum w amplitude detected above the mountains. w_{bp} is interpolated along these directions. The "actual" horizontal wave vector (k_h) direction of propagation should be parallel to that in which $k_h(\lambda_h)$ is maximum(minimum). This extreme is observed between -10 and -5 deg. For other values, λ_h increases again. This procedure allows the estimation of horizontal propagation directions from horizontal experimental or numerical data.

3.2. Case 2 (54S)

In this case, an anticyclonic flow near the surface is present over the whole continental zone while a large amplitude ridge is observed in the upper troposphere. Over the Drake

Passage, a transition region between a cyclonic circulation to the East and the mentioned anticyclone over the West at low levels is present. As a result, it is possible to distinguish a low level and upper level flow entering the continent from SW (Figures 5a to 5d). This flow forces large amplitude stationary MWs with amplitudes around 3m/s near to the southern tip of the Andes Range (Figures 6a-b). In this case, the "apparent" λ_h is between 60 and 70 km (Figure 6c), due to the slanted ZP respect to the actual horizontal wave propagation direction, with a significant meridional component. This direction may be determined as shown in 3.1 (omitted for brevity).

3.3. Case 3 (59S)

A low level pressure system is located over South of Argentina, with its center over the Drake Passage (Figure 7a). In the upper troposphere, a long wave trough with its axis over the continent is in phase with this low pressure system, suggesting that this case consists in a barotropic cyclone. As a result, the wind field does not show strong variations neither in intensity nor in rotation between lower and upper levels of the troposphere. Both lower and upper level associated circulations present a NW-SE flow (Figures 7b to 7d). This is the most significant case detected above the Drake Passage during winter 2009. MWs are practically not observed in this region. A linear structure of GWs at 600 hPa from NW to SE (Figures 8a) possibly generated by the considerable vertical shear in u (Figure 8b), is observed.

3.4. Case 4 (65S)

The South Pacific subtropical anticyclone penetrates the continent from the South while a low pressure system leaves the Drake Passage during its eastward displacement (Figure

9a). The upper level field is in phase with i) the low level circulation on the western side of South America where a ridge over a high pressure system is located and ii) a relative upper low pressure lying over the low pressure system at the SE of South America (Figures 9b to d). The flow at 600 hPa from SE over the Antarctic Peninsula generates intense MWs in NW-SE direction with amplitudes larger than 3 m/s (Figures 10a-b), predominant λ_h values around 60 km and long λ_z (Figure 10c). This structure persists at 200 hPa, while at 50 hPa the waves seem to encounter a critical layer as an abrupt rotation of the mean wind with increasing height takes place.

3.5. Case 5 (71S)

The Atlantic Subtropical anticyclone is positioned over the continental zone, with its southern flank over the Drake Passage, yielding a strong low level flow from West at all tropospheric levels (Figures 11a to d). At upper levels a similar configuration with a strong ridge at 200 hPa is present. A more complex MWs distribution is observed in this region. Two dominant MW modes with λ_h ranging between 60 and 70 km (CWT at 600 hPa) and long λ_h are observed (Figures 12a to c).

4. Vertical Flux of Zonal Momentum

We now consider with some detail case 1. We first calculate the zonal component of vertical flux of horizontal momentum (M_x) resulting from the above simulations. It deserves to be mentioned here that momentum and a sometimes used another variable, the pseudomomentum, are distinct but related quantites that appear in wave-mean interaction theory. Conservation of momentum is related to translational invariance of the physics, whereas conservation of pseudomomentum is related to translational invariance of the medium in which the waves propagate. The relevant components of their respective fluxes, i.e., the vertical fluxes of horizontal momentum and pseudomomentum, are equal, to sufficient level of approximation, in this problem. The pseudomomentum flux can be equated to the vertical group velocity times the horizontal pseudomomentum density [*Warner and McIntyre*, 1996; 1999].

The topographic height as well as the ground pressure distribution along each racetrack are considerably asymmetric in the zonal direction. M_x calculated over a length L, for middle and high intrinsic GWs, is defined as [*e.g. Nappo*, 2002; *Fritts and Alexander*, 2003]:

$$M_x = -\overline{\rho_0}(\overline{uw}) = -L^{-1}\overline{\rho_0}\int_{-L/2}^{+L/2}(uw)dx \quad (1)$$

We can take for L a representative scale of the ridge width or of the generated waves. In the case of a monochromatic wave, unless the wave breaks down or undergoes dissipation, the stress associated with it is expected to be constant with height. This result does not require the background flow to be constant with height too. The wave stress remains uniform and the total vertical flux of wave energy varies with height in proportion to u_0, except where $u_0 = 0$ [*e.g. Nappo*, 2002].

In case 1, M_x is calculated at constant pressure levels every 50 hPa between 500 and 50 hPa. We do not consider levels below 500 hPa due to missing simulated data below the mountains top relief. Considering the maximum width of region 1, the wave perturbations are band-pass filtered with cutoffs between i) $\lambda_x = 8$ and 360 km and ii) 70 and 130 km. The first choice considers a broad spectrum of GWs whereas in the second choice it is intended to isolate the main MW mode, observed around 100 km with CWT (Figure 4). We identify i) and ii) selections with the upper indexes C and 100, corresponding to the "complete" GW spectra retained along racetrack 1 and the 100 km mode, respectively. To test the expected variability near to and far from the mountains, we separate the integration in (1) along racetrack 1 into eastern and western segments ($M_{x,E}$ and $M_{x,W}$) respectively, including for completeness the integration along the complete racetrack ($M_{x,T}$) (Figure 13). This last is equivalent to the average between eastern and western contributions. With this notation, for example M_x for the 100 km mode and eastern segment is denoted as $M_{x,E}^{100}$. For briefness, we only show M_x results corresponding to racetrack 1. This selection is made from the outstanding w amplitude distribution observed in Figure 3. We see the following features (Figure 14): i) $M_{x,T}^{C}$, $M_{x,E}^{C}$ and $M_{x,O}^{C}$ decrease continuously from large values at 500 hPa (-900, -700 and -500 mPa, respectively) to considerably smaller at 50 hPa (-126, -47 and +33 mPa), revealing a progressive deposition of momentum with increasing altitude, with the exception of a short height interval between 200 and 300 hPa where these parameters remain uniform; ii) $M_{x,T}^{100}$, $M_{x,E}^{100}$ and $M_{x,O}^{100}$ exhibit a similar relative behavior, with considerably smaller values, ranging from -168, -120 and -71 hPa at 500 hPa down to -37, -11 and +15 mPa at 50 hPa, respectively; iii) this behavior is in agreement with theoretical results [*Ern et al*, 2004] and it must be mainly attributed to waves with short λ_x (in this case, shorter than 100 km); iv) M_x as well as it vertical derivative is, in all cases, considerably larger near to than far from the mountains; v) in the eastern segment it seems that neither critical levels nor wave dissipation effects far from the mountains take place; vi) the absolute vale of momentum flux (M_T^C), calculated from the zonal and the meridional component ($M_{y,T}^C$), decreases from -910 mPa at 500 hPa to -48 mPa at 50 hPa and is very similar to $M_{x,T}^C$. This is expected, from the prevailing wind and mountain range alignment at 49S. Different segments along racetrack

1 yielded slight differences with the above results. For brevity, $\boldsymbol{M}$ corresponding to the 4 remaining cases will be discussed in a future work. Noteworthy features observed in case 4 (65S) appear very different respect to case 1 and deserves to be briefly commented. Just below the northern Antarctic Peninsula tip, a strong variability below 250 hPa in the zonal, meridional and absolute value of $\boldsymbol{M}$, is observed in comparison with case 1. Above this level, the high $\boldsymbol{M}$ values observed below become suddenly negligible. This is expected from the positive/negative mean zonal background wind below/above 200 hPa, which exhibits a strong wind rotation at higher pressure levels. Critical level dissipation, breaking, reflection and refraction effects due to the background wind variability explain this behavior.

5. Conclusions

The 5 cases study considered along Southern Andes Range, Drake Passage and its prolongation in the Antarctic Peninsula reveal the following features:

- systematic large amplitude, stationary GW wave structures, forced by the mountains up to the stratosphere and persistent during several hours;
- CWT analysis at uniform pressure levels is adequate for MW simulations;
- one or at most two prevailing modes of oscillation, after applying CWT at constant latitudes and pressure levels;
- in all cases, the prevailing modes are characterized by short horizontal ($\leq$ 100 km) and long vertical wavelengths ($>$ 8 km);
- for each of the 5 cases considered, different cyclonic-anticyclonic circulation at low levels as well as geopotential distributions at high levels were observed;

- during the 3 months period considered in the simulations, 97 synoptic hours were affected by a low pressure system in the region, nevertheless, this period was not sufficient to draw general conclusions linking synoptic conditions with MWs generation;

- the analysis of one representative case revealed a large and variable $\boldsymbol{M}$ distribution with height, in which the contribution to $\boldsymbol{M}$ due to the short horizontal wavelengths of the spectrum is larger than the transported by the prevailing mode, in agreement with theoretical results;

- a comparison of our results with previous experimental results is not straightforward, as it depends on the observational technique and on the space and/or time averaging selected by other authors (a very limited number of single events are reported);

- the complete period analyzed indicates that the 5 racetracks proposed for the SAANGRIA experiment are representative of the typical mountain wave morphology in the region.

We expect that simulations from several winters, still being processed and analyzed, will draw further conclusions regarding possible interannual and regional systematic features during the systematic generation and propagation of MWs in this region.

Acknowledgments. Manuscript prepared under grants UBA X004, CONICET PIP 5932 and ANPCyT PICT 1999. A. de la Torre and P. Alexander are members and P. Llamedo holds a fellowship of CONICET. The GFZ contribution was partially funded through DFG priority program CAWSES SPP 1176. We acknowledge data provided by the NOAA-CIRES/Climate Diagnostics Center, Boulder (CO) from their website www.cdc.noaa.gov.

References

Alexander, M.J., and H. Teitelbaum (2007), Observation and analysis of a large amplitude mountain wave event over the Antarctic peninsula, *J. Geophys. Res.*, **112**, D21103, doi:10.1029/2006JD008368.

Alexander, M.J., et al. (2008), Global estimates of gravity wave momentum flux from High Resolution Dynamics Limb Sounder observations, *J. Geophys. Res.*, **113**, D15S18, doi:10.1029/2007JD008807.

de la Torre, A., P. Alexander, P. Llamedo, C. Menéndez, T. Schmidt, and J. Wickert (2006), Gravity waves above the Andes detected from GPS radio occultation temperature profiles: Jet mechanism?, *Geophys. Res. Lett., **33***, L24810, doi:10.1029/2006GL027343.

Ern, M., P. Preusse, M.J. Alexander, and C.D. Warner (2004), Absolute values of grav491 ity wave momentum flux derived from satellite data, *J. Geophys. Res.*, **109** (D20103), 492 doi:10.1029/2004JD004,752.

Fritts, D.C., and M.J. Alexander (2003), Gravity wave dynamics and effects in the middle atmosphere, *Rev. Geophys.*, **41**(1), 1003, doi:10.1029/2001RG000106.

Fritts, D.C., R.B. Smith, J.D. Doyle, and S. Eckermann (2010), Overview of the Southern AndesANtarctic GRavity wave InitiAtive (SAANGRIA), *14th Conf. on Mountain Meteorology*, (https://confex.webex.com/cmp0306lc/webcomponents/docshow/ docshow.do?siteurl=confexsetupStatus=1)

Gill, A.E., (1982), *AtmosphereOcean Dynamics*. Academic Press, 662 pp.

Hamming, R.W. (1998), *Digital Filters, 3rd ed.*, Dover Publications, Mineola, New York.

Hertzog, A., G. Boccara, R.A. Vincent, F. Vial, P. Cocquerez, (2008), Estimation of gravity wave momentum flux and phase speeds from quasi-Lagrangian stratospheric balloon flights. Part II: Results from the Vorcore campaign in Antarctica, *J. Atmos. Sci.*, **65** (10), pp. 3056-3070.

Nappo, C.J. (2002), *An Introduction to Atmospheric Gravity Waves*, Int. Geophys. Ser., **85**, 276 pp., Academic, San Diego, Calif.

Plougonven, R., A. Hertzog, and H. Teitelbaum (2008), Observations and simulations of a large-amplitude mountain wave breaking over the Antarctic Peninsula , *J. Geophys. Res.* , **113** , D16113, doi:10.1029/2007JD009739.

Preusse, P., S.D. Eckermann, and M. Ern (2008), Transparency of the atmosphere to short horizontal wavelength gravity waves, *J. Geophys. Res.*, **113**, D24104, doi:10.1029/2007JD009682.

Smith, R.B. (1979), The influence of mountains on the atmosphere. *Adv. Geophys.* 21, 87230.

Smith, R.B., B.K. Woods, J. Jensen, W.A. Cooper, J.D. Doyle, Q. Jiang, and V. Grubii (2008), Mountain Waves Entering the Stratosphere. *J. Atmos. Sci.*, **65**, 25432562.

Skamarock, W.C., J.B. Klemp, J. Dudhia, D.O. Gill, D.M. Barker, M. Duda, X.-Y. Huang, W. Wang, and J.G. Powers (2008), A Description of the Advaced Research WRF Version 3, NCAR Technical note NCAR/TN-475+STR.

Shutts, G.J., M. Kitchen, and P.H. Hoare (1988), A large amplitude gravity wave in the lower stratosphere detected by radiosonde, '*Q. J. Roy. Meteor. Soc., 114*, 579-594.

Shutts, G.J., S.B. Vosper (2011), Stratospheric gravity waves revealed in NWP model forecasts, *Q. J. Roy. Met. Soc.*, **137** (655), pp. 303-317.

Vincent, R.A. and I.M. Reid (1983), HF Doppler measurements of mesospheric momentum fluxes, *J.Atmos. Sci*,**40**, 1321-1333.

Vincent, R.A., A. Hertzog, G. Boccara, and F. Vial (2007), Quasi-Lagrangian superpressure balloon measurements of gravity-wave momentum fluxes in the polar stratosphere of both hemispheres, *Geophys. Res. Lett.*, **34**, L19804, doi:10.1029/2007GL031072.

von Storch, H., H. Langenberg and F. Feser (2000), A spectral nudging technique for dynamical downscaling purposes, *Mon. Weather Rev.*, **128**, 3664 3673

Wang, L., and M.J. Alexander (2010), Global estimates of gravity wave parameters from GPS radio occultation temperature data, J. Geophys. Res., 115, D21122, doi:10.1029/2010JD013860.

Warner, C.D. and M.E. McIntyre (1996), On the propagation and dissipation of gravity wave spectra through a realistic middle atmosphere, *J. Atmos. Sci.*, **53**, 22, 3213-3235.

Warner, C.D. and M.E. McIntyre (1999), Toward an ultra-simple spectral gravity wave parameterization for general circulation models, *Earth Planets Space*, **51**, 475-484.

Wu, D.L., P. Preusse, S.D. Eckermann, J.H. Jiang, M. de la Torre Juarez, L. Coy, B. Lawrence, and D.Y. Wang (2006), Remote sounding of atmospheric gravity waves with satellite limb and nadir techniques, *Adv. Space Res.*, **37**, 22692277.

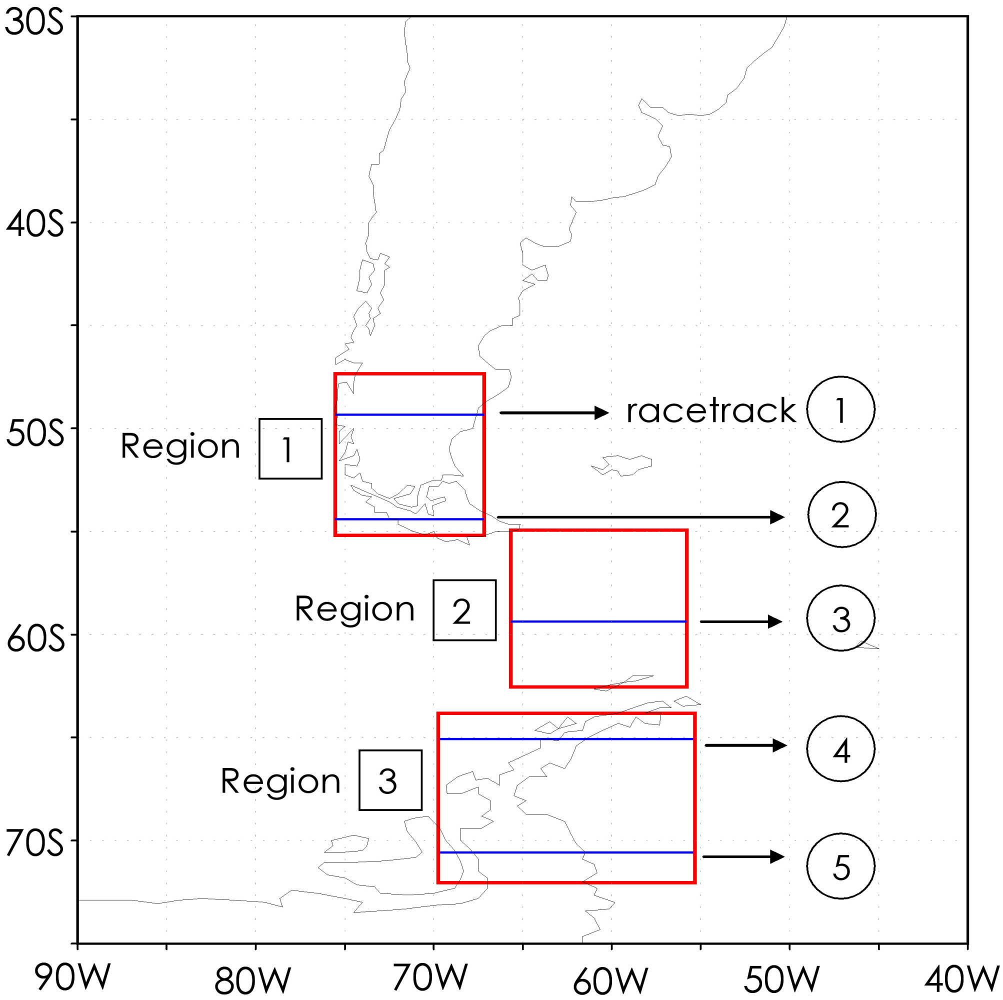

Figure 1. The three considered regions for the numerical simulations and 5 W-E proposed aircraft racetracks during the SAANGRIA experiment above mountain tops and the Drake Passage (see text).

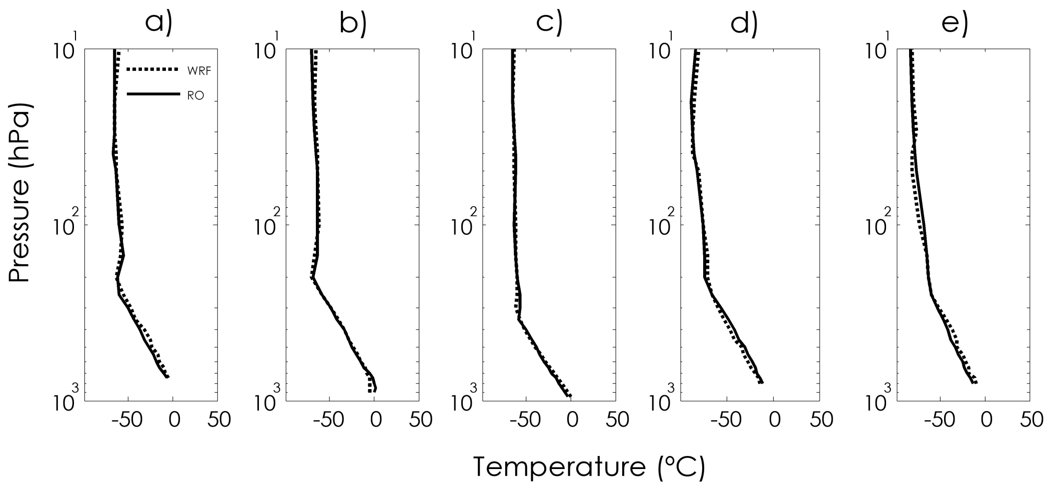

Figure 2. *T* RO profiles retrieved from COSMIC, for validation of cases a) 1, b) 2, c) 3, d) 4 and e) 5. Time/average position of the 5 RO events are, respectively: 16 June 08Z/lat=-51,65 lon=-73,96; 25 June 18Z/lat=-53,11 lon=-74,45; 21 June 09Z/lat=-55,41 lon=-64,87; 19 July 12Z/lat=-67,27 lon=-65,04 and 28 July 19Z lat=-68,64 lon=-67,65.

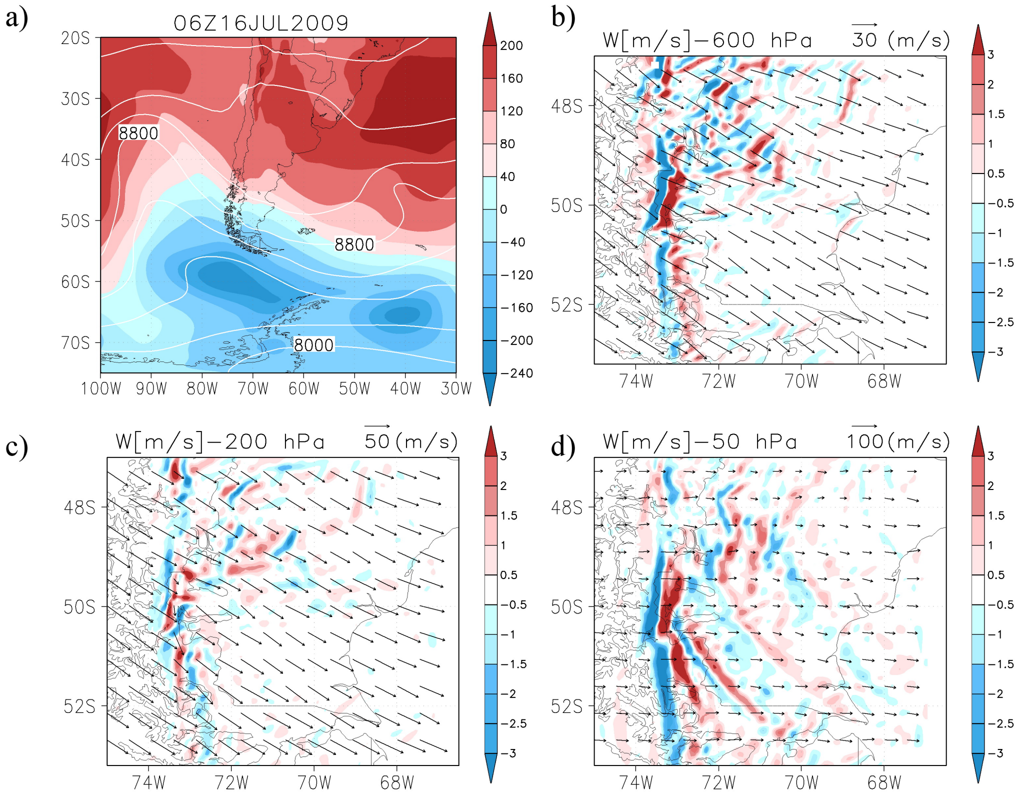

Figure 3. *Case 1*: a) 1000 and 200 hPa geopotential height (shadow regions and thick lines, respectively). b) to d) u and w at 600, 200 and 50 hPa levels respectively.

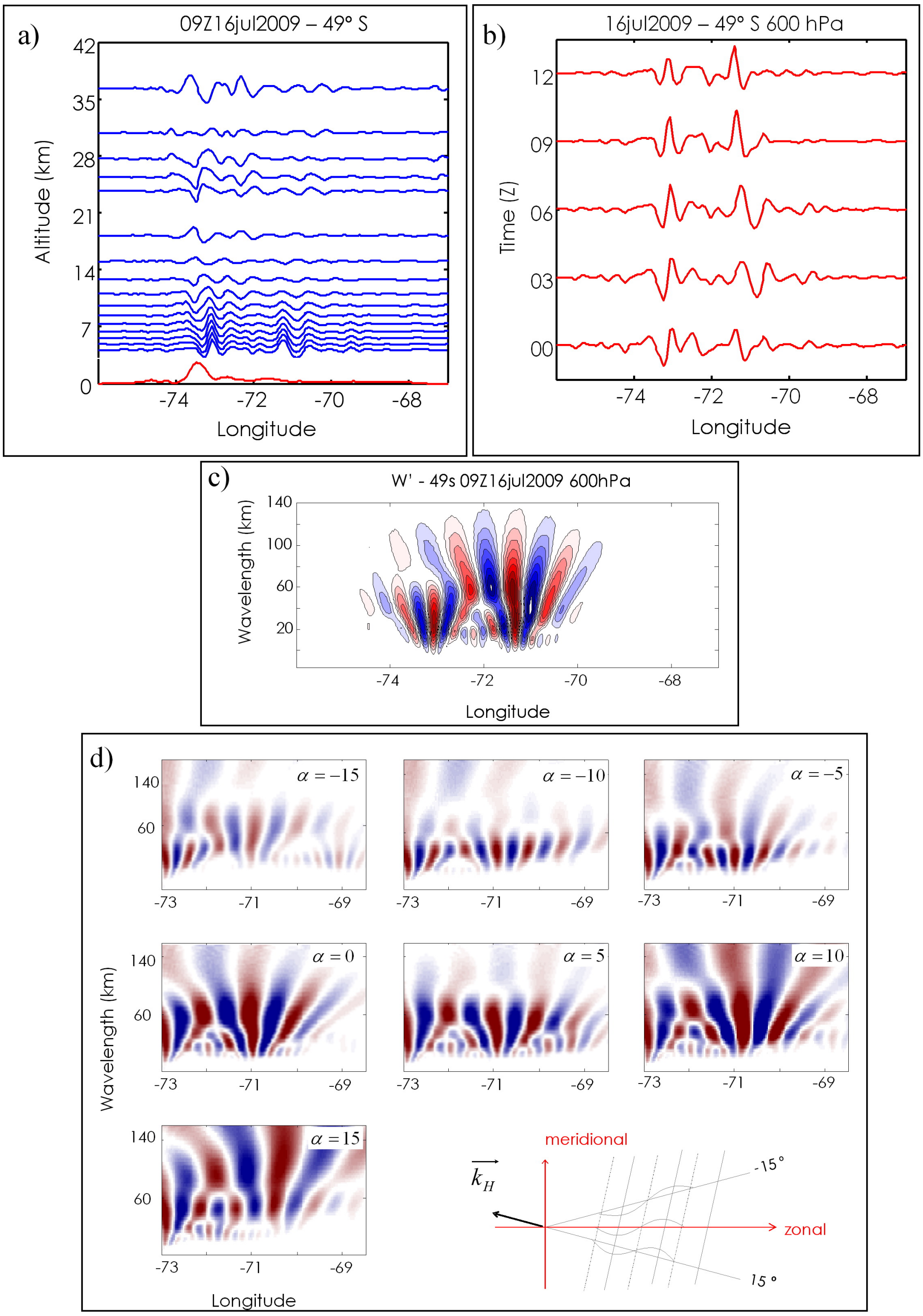

Figure 4. *Case 1 (cont)*: w as a function of a) altitude and b) time, c) w CWT at 600 hPa and racetrack 1, d) CWT variation along seven arbitrary consecutive directions of w (see bottom right). The direction $\alpha = 0$ coincides with c).

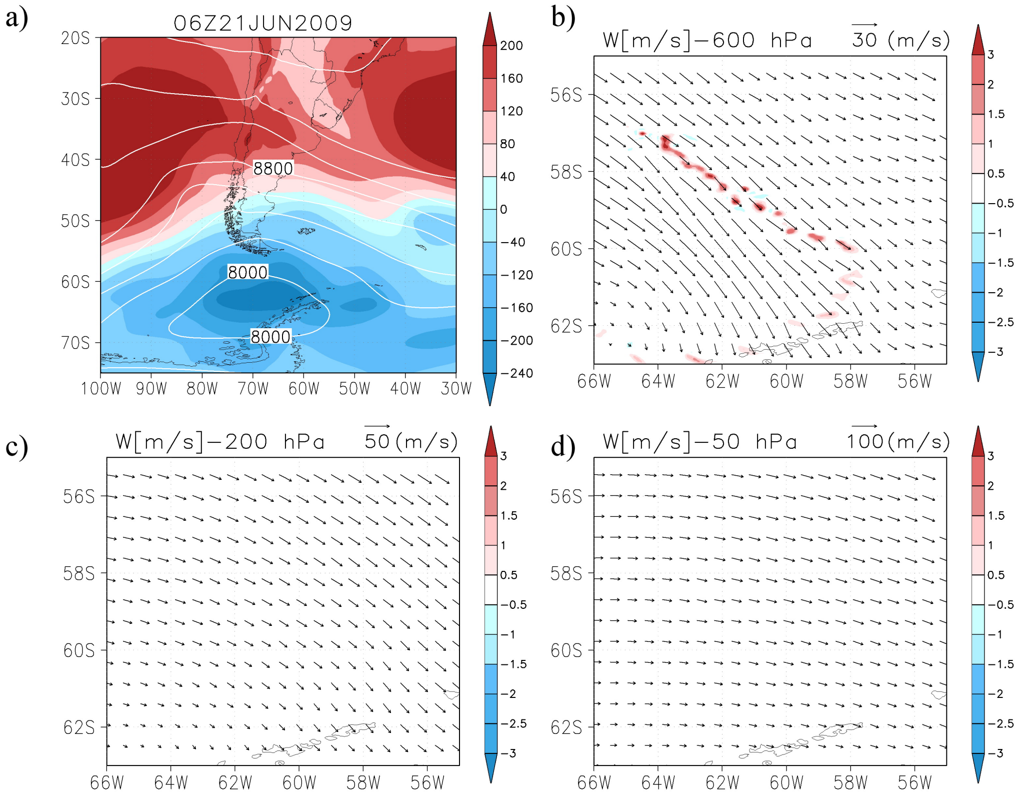

Figure 5. *Case 2*: The same description as in Figure 3.

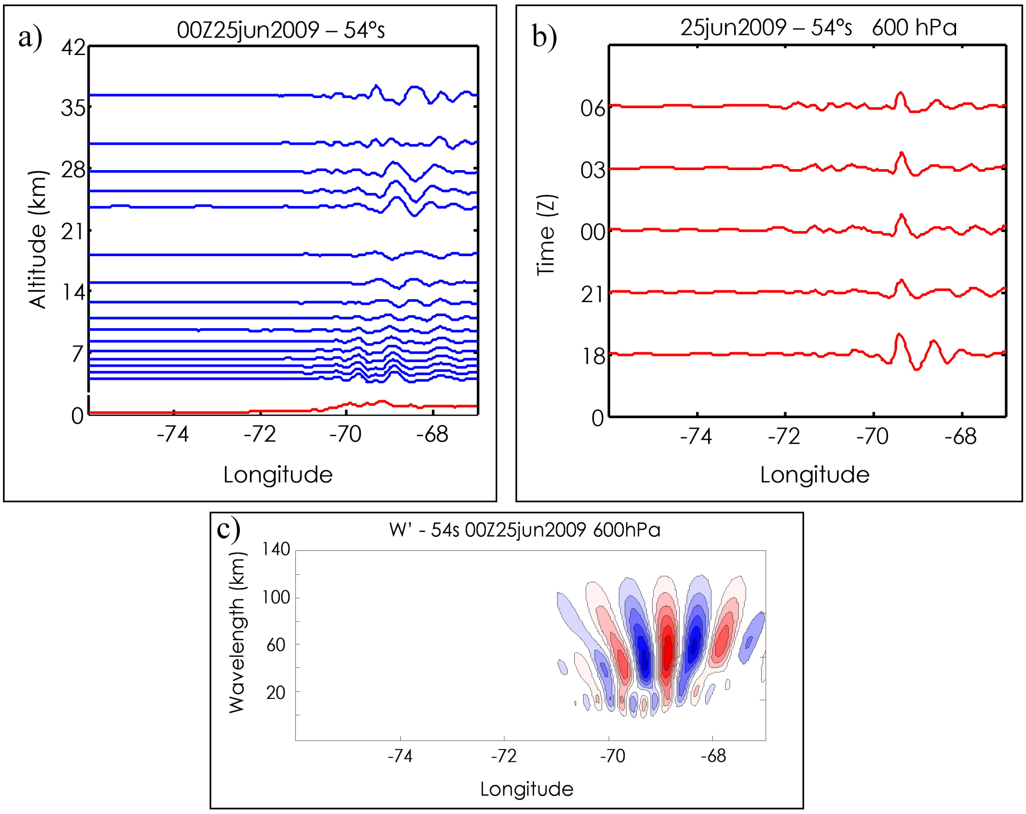

Figure 6. *Case 2*: w as a function of a) altitude and b) time, c) w CWT at 600 hPa and racetrack 2.

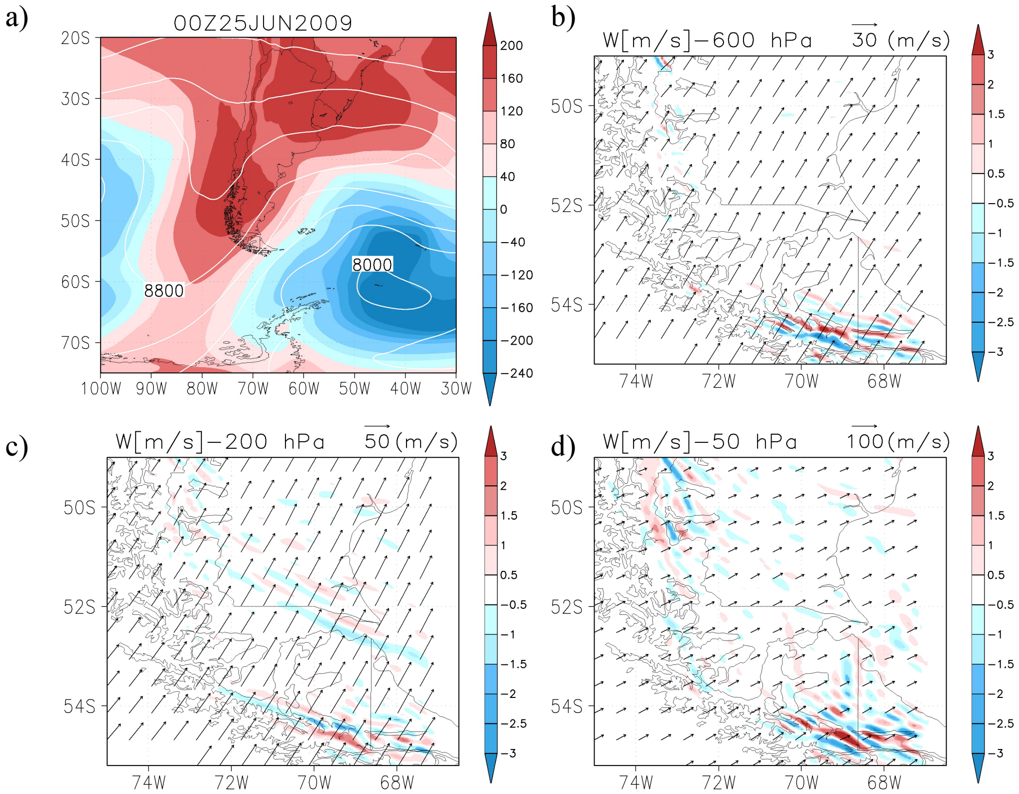

Figure 7. *Case 3*: The same description as in Figure 3.

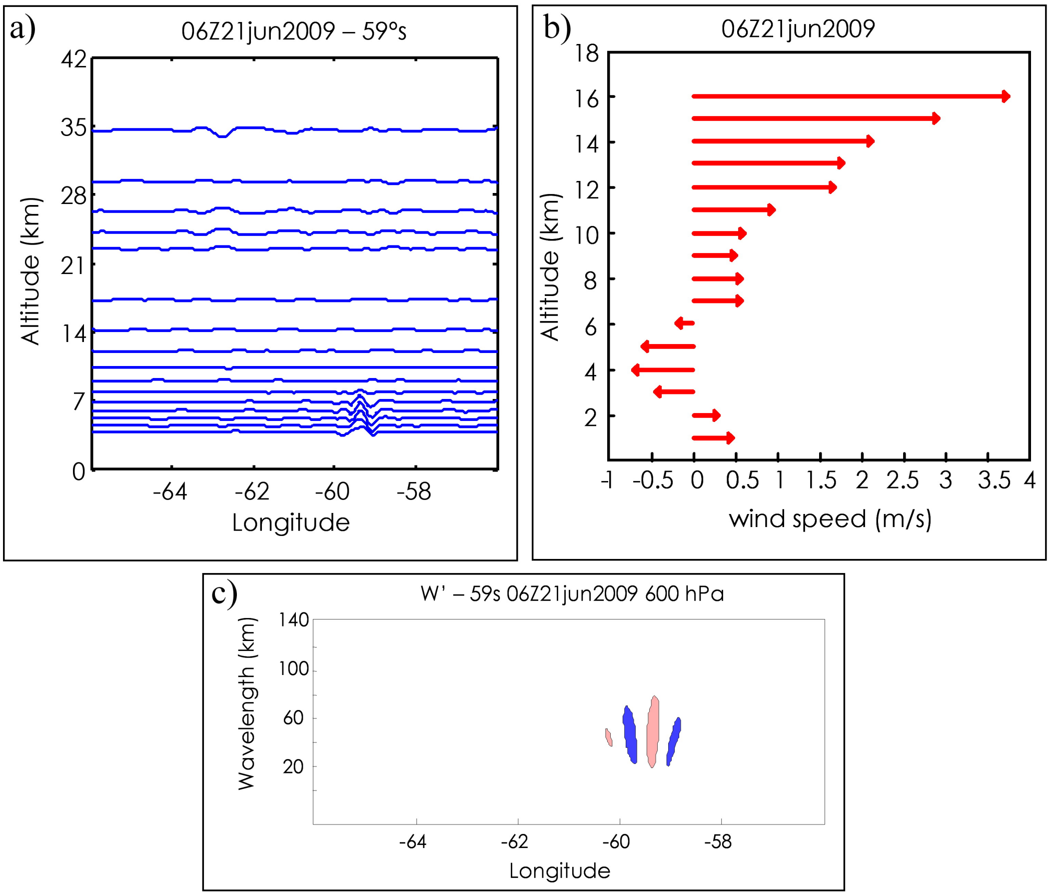

Figure 8. *Case 3*: a) w and b) u as a function of altitude and c) w CWT at 600 hPa and racetrack 3.

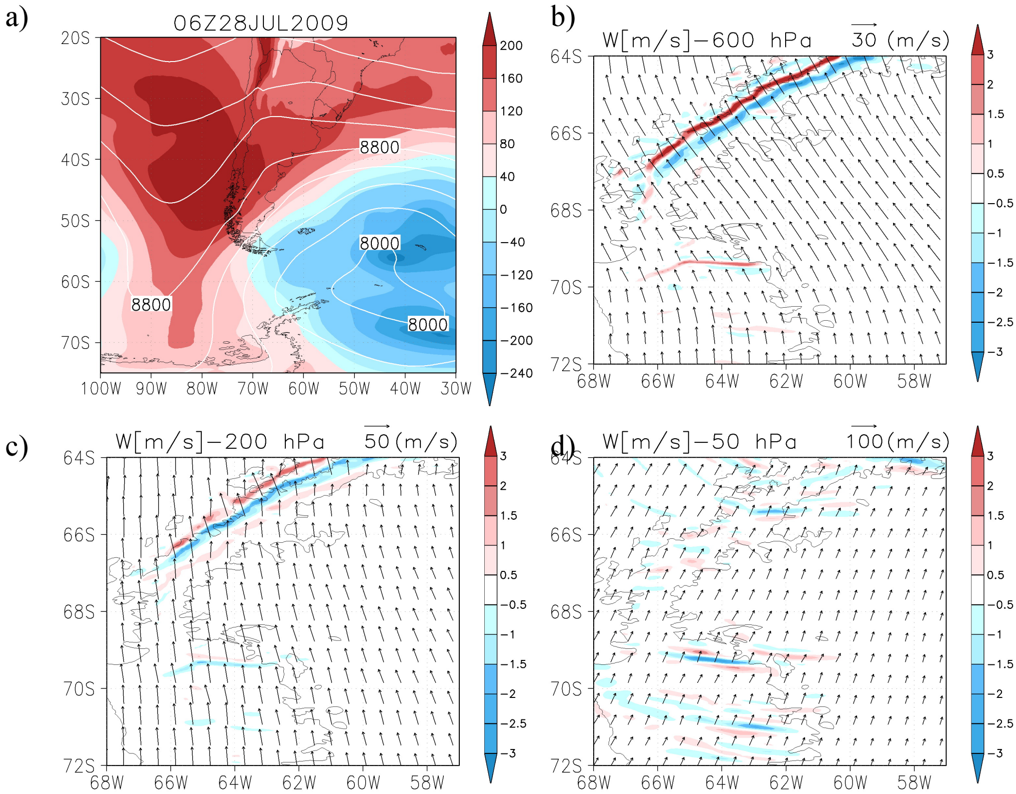

Figure 9. *Case 4*: The same as Figure 3a-d

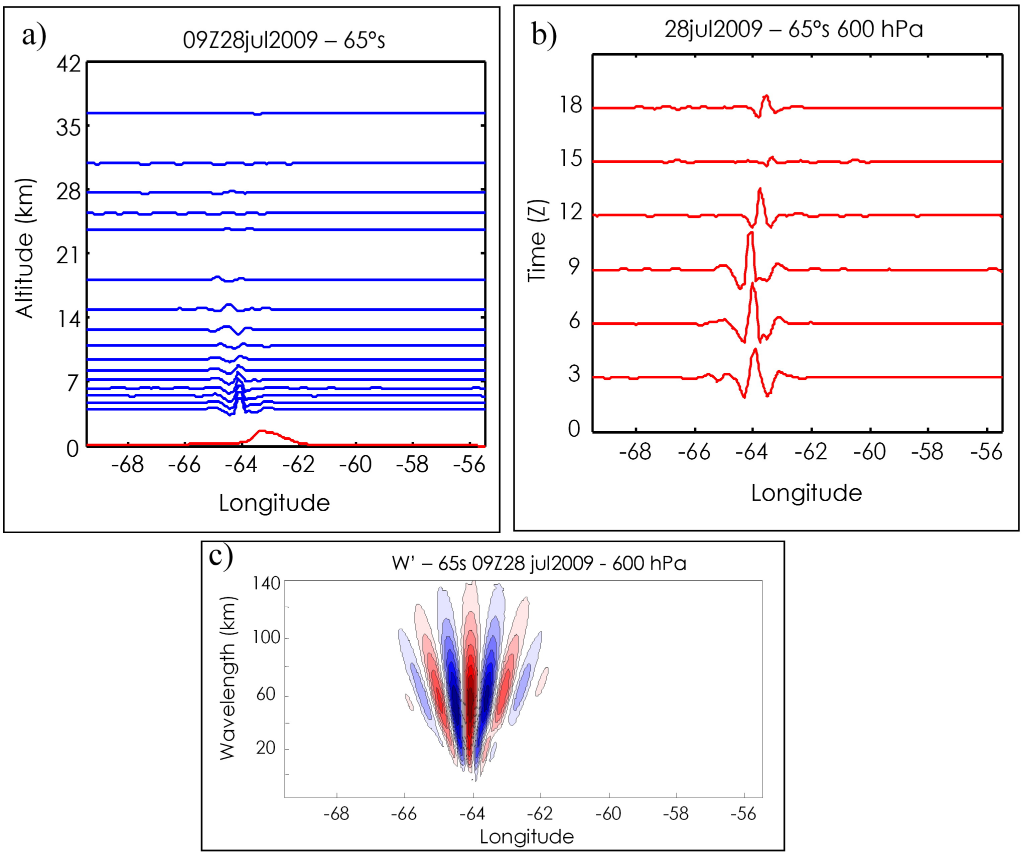

Figure 10. *Case 4*: w as a function of a) altitude and b) time, c) w CWT at 600 hPa and racetrack 4.

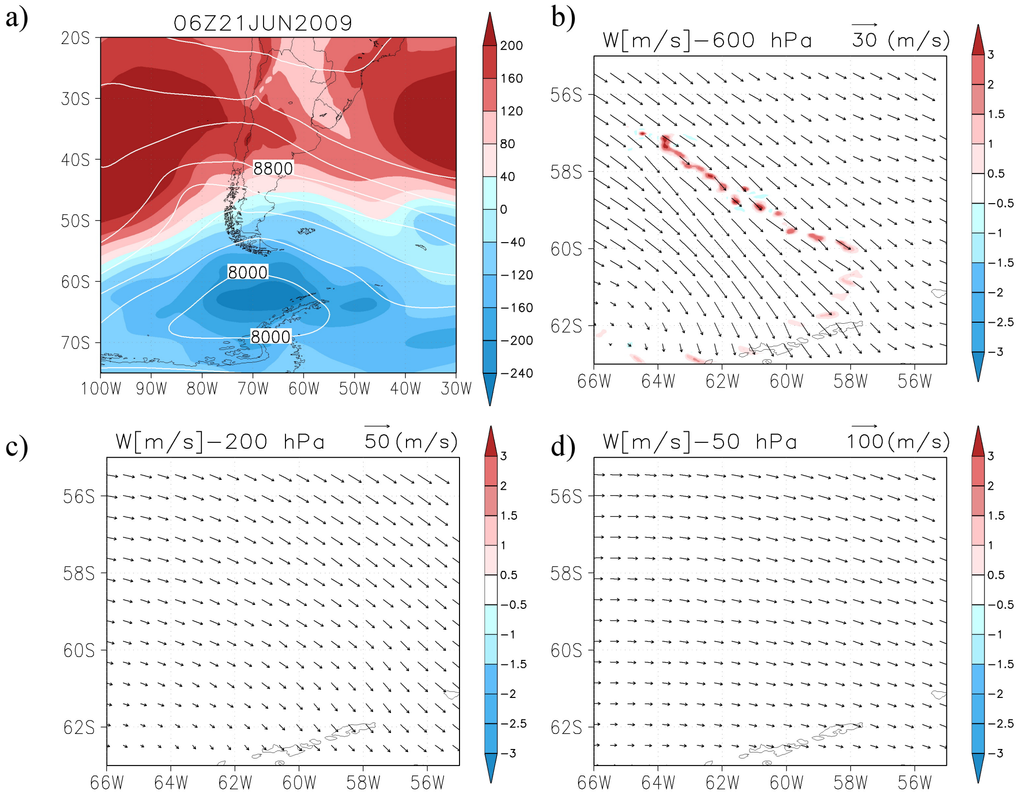

Figure 11. *Case 5*: The same as Figure 3a-d

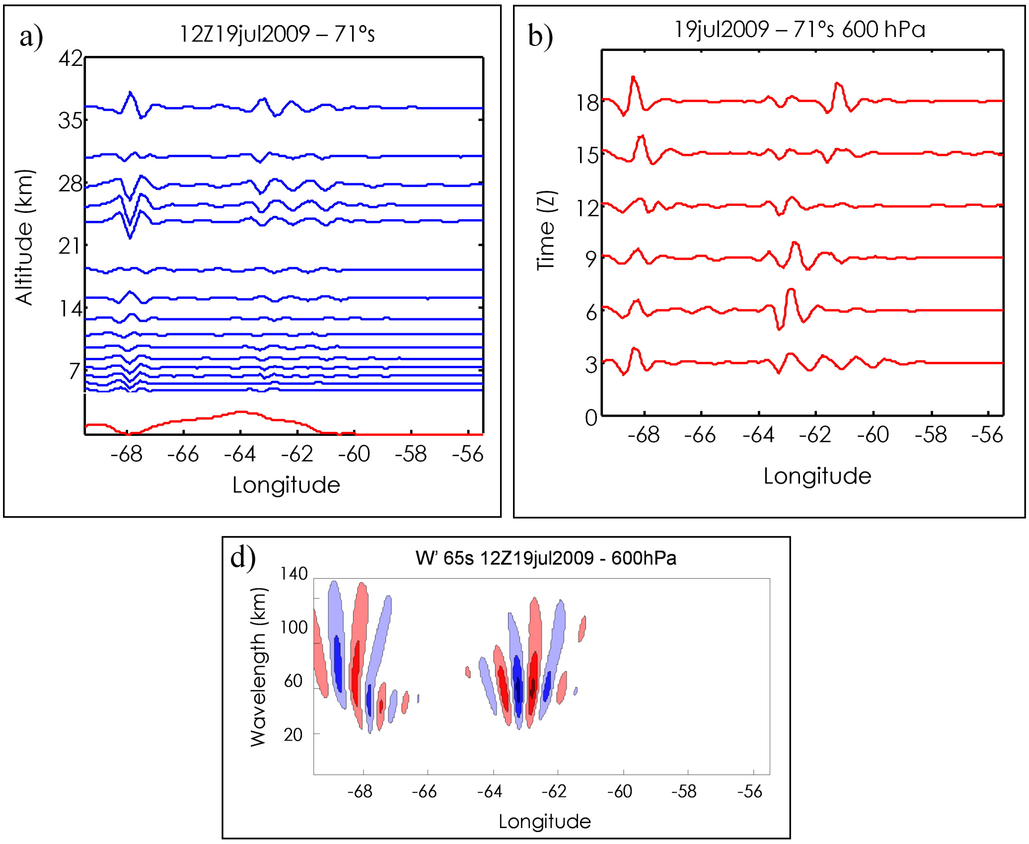

Figure 12. *Case 5*: w as a function of a) altitude and b) time, c) w CWT at 600 hPa and racetrack 5.

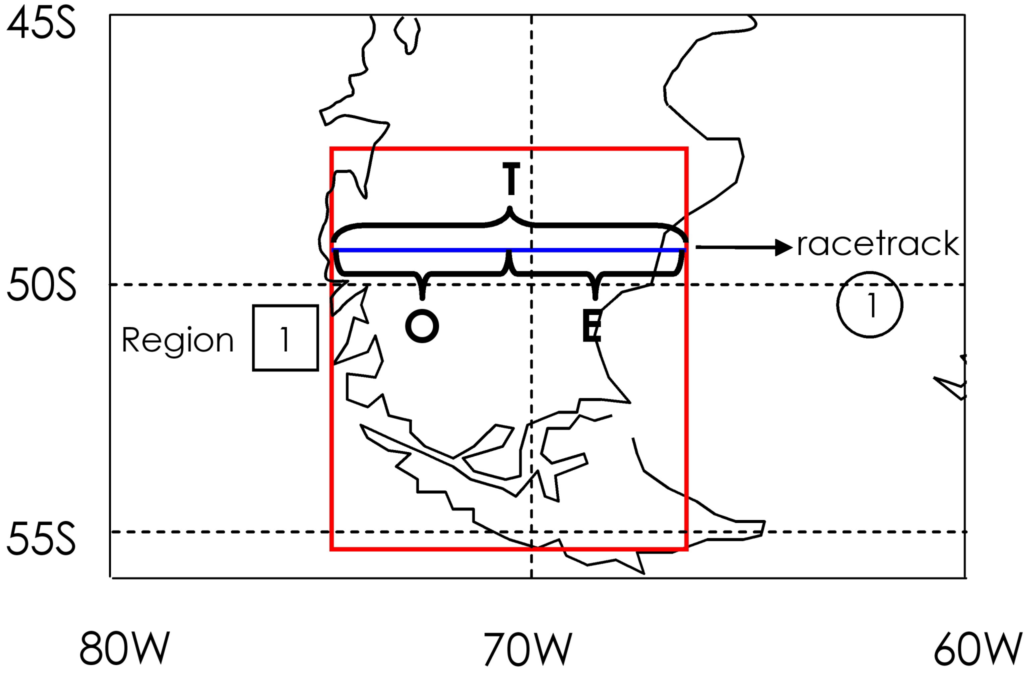

Figure 13. Three different segments for the integration of M_x: $M_{x,E}$, $M_{x,W}$ and $M_{x,T}$ along racetrack 1 (Case 1).

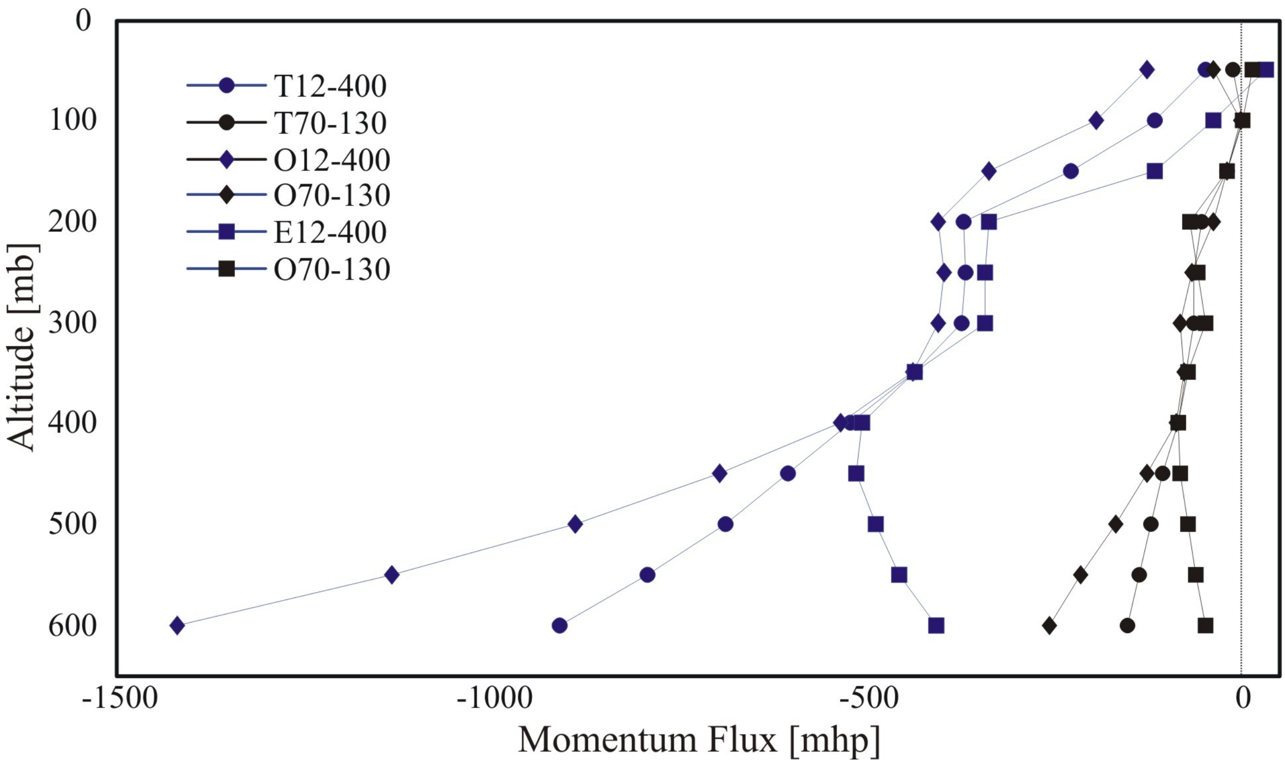

Figure 14. $M_{x,E}$, $M_{x,W}$ and $M_{x,T}$ along racetrack 1 (Case 1) for the two pairs of cutoffs selected. These are denoted with the upper indexes C and 100 (see text), corresponding to the "complete" GW spectra and the mode of $\lambda_x = 100$ km, respectively. The absolute value of M_T